Supplementary Information for

Out-of-plane dipole-modulated photogenerated carrier separation and recombination at Janus-MoSSe/MoS_2 van der Waals heterostructure interfaces: Ab initio time-domain study

Xiangyue Liu[1,2*], Huadong Zeng[3*], Guangzhao Wang[4], Xinlu Cheng[5,6], Shengyuan A. Yang[2†], and Hong Zhang[1,5‡]

[1]*College of Physics, Sichuan University, Chengdu 610065, China*

[2]*Research Laboratory for Quantum Materials, Singapore University of Technology and Design, Singapore 487372, Singapore*

[3]*School of Materials and New Energy, South China Normal University, Shanwei 516625, China*

[4]*Key Laboratory of Extraordinary Bond Engineering and Advanced Materials Technology of Chongqing, School of Electronic Information Engineering, Yangtze Normal University, Chongqing 408100, China.*

[5]*Key Laboratory of High Energy Density Physics and Technology of Ministry of Education, Sichuan University, Chengdu 610065, China*

[6]*Institute of Atomic and Molecular Physics, Sichuan University, Chengdu 610065, China*

1. Nonadiabatic Molecular Dynamics combined with Time-Dependent Density Functional Theory

Ab initio nonadiabatic molecular dynamics (NAMD) simulations enable the description of the excited-state carrier dynamics in multiple dimensions, including real

* These authors contributed equally to this work.
† Corresponding author: Shengyuan A. Yang, email: shengyuan_yang@sutd.edu.sg
‡ Corresponding author: Hong Zhang, email: hongzhang@scu.edu.cn

space, momentum space, energy as well as in the timescale.[1] All the excited-state real-time TDDFT simulations of photoinduced ultrafast carrier separation and carrier recombination at the interface of Janus-MoSSe/MoS_2 heterostructures are performed adopting the mixed quantum-classical Fewest-Switch surface hopping (FSSH) and decoherence-induced surface hopping (DISH) technique.[2-4] The time-dependent charge density can be obtained by the sum of the densities of occupied single-particle Kohn-Sham (KS) orbitals $\Psi_p(\boldsymbol{r},t)$:[5]

$$\rho(\boldsymbol{r},t)=\sum_{p=1}^{N_e}\left|\Psi_p(\boldsymbol{r},t)\right|^2 \tag{1}$$

where N_e denotes the total number of electrons. The electron density evolution is characterized by time-dependent variational principle to the KS energy, generating a set of single-electron equations for the evolution of KS orbitals:[6, 7]

$$i\hbar\frac{\partial\left|\Psi_p(\boldsymbol{r},t)\right\rangle}{\partial t}=\widehat{H}(\boldsymbol{r},\boldsymbol{R},t)\left|\Psi_p(\boldsymbol{r},t)\right\rangle \tag{2}$$

A set of adiabatic KS basis $\left\{\left|\psi_i\left(r,R(t)\right)\right\rangle\right\}$ is adopted to expand the time-dependent KS orbitals：

$$\begin{aligned}\left|\Psi_p(\boldsymbol{r},t)\right\rangle&=\sum_i\left|\psi_i\left(r,R(t)\right)\right\rangle\left\langle\psi_i\left(r,R(t)\right)\middle|\Psi_p(\boldsymbol{r},t)\right\rangle\\&=\sum_i c_i(t)\left|\psi_i\left(r,R(t)\right)\right\rangle\end{aligned} \tag{3}$$

where $c_i(t)$ is correspond to the expansion coefficients. The square modulus of the expansion coefficients, $|c_i(t)|^2$, represent the occupation of excited carriers on the corresponding Kohn-Sham orbitals. By inserting eq (3) to eq (2), the equation for the evolution of the adiabatic basis expansion coefficient can be obtained:

$$i\hbar\frac{\partial c_i(t)}{\partial t}=\sum_j c_j(t)\left(\varepsilon_j\delta_{ij}+d_{ij}\right) \tag{4}$$

in which ε_j is the eigenvalue of the $\left|\Psi_p(\boldsymbol{r},t)\right\rangle$ KS orbitals, d_{ij} is the nonadiabatic coupling (NAC) between the states i and j,[8-10] given by:

$$d_{ij} = \left\langle \varphi_i \middle| \frac{\partial}{\partial t} \middle| \varphi_j \right\rangle = \sum_I \frac{\langle \varphi_i | \nabla_R H | \varphi_j \rangle}{\epsilon_i - \epsilon_j} \cdot \dot{R}_I \quad (5)$$

Nonadiabatic coupling (NAC) strength is responsible for the probability of transition between adiabatic states during the ultrafast carrier transfer and nonadiabatic electron-hole recombination processes, which is strongly related to the electron-phonon coupling. According to the eq (5), NAC is determined by electron-phonon coupling matrix element $\langle \varphi_i | \nabla_R H | \varphi_j \rangle$, the energy difference of initial and final states $\epsilon_i - \epsilon_j$ and the nuclear velocity $\dot{R}_I$. the NAC is proportional to the e-p coupling and nuclear velocity and inversely proportional to the energy difference.

Within the scheme of surface hopping method, the classical nuclear trajectory propagating on a single Born-Oppenheimer (BO) potential energy surface has a restricted probability to hop to another potential surface, so that the transitions between electronic states can be simulated directly. The nature of the surface hopping can be revealed by the stochastic hopping algorithm, thus abundant trajectories are required to demonstrated fast transitions between the potential energy surface. The frequently-used strategy to perform a hopping in surface hopping simulation allows surface hops to occur at any time step that avoid the complexity of searching the critical hopping point. On one hand, Prezhdo *et al* develop a scheme where adiabatic Kohn-Sham orbitals are used to expand the electronic wavefunction.[11] Under the single particle approximation, complex many-body interactions between nuclei and electrons can be simplified to the single particle approximation. On the other hand, for a condensed matter system containing a large number of atoms, the effect of exciting one electron on the nucleus structure is negligible compared to the thermal perturbation effect. Given that by introducing the classical path approximation (CPA),[12, 13] the nuclear trajectory set on excited electronic states can be replaced by a pre-determined ground electronic state trajectory. Consequently, the velocity rescaling in FSSH is substituted by multiplying the hopping probability with the Boltzmann factor to satisfy the energy conservation:

$$P_{i\to j}(t, \Delta t) = P_{i\to j}^{FSSH}(t, \Delta t) \cdot b_{i\to j}(t) \quad (6)$$

$$b_{i\to j}(t) = \begin{cases} exp\left(\frac{\epsilon_i - \epsilon_j}{k_B T}\right), & \epsilon_i > \epsilon_j \\ 1, & \epsilon_i \leq \epsilon_j \end{cases} \quad (7)$$

FSSH-CPA requires only one nuclear trajectory in the ground state to generate averaged surface hopping results. Many studies have confirmed the reliability of FSSH-CPA.[2, 13-15] It is noted that although CPA can save a lot of computing costs and be as a reasonable approach for rigid structures such as interfaces, organic and inorganic configurations, under the CPA approximation the evolution of classical and quantum degrees of freedom are independent of each other without the consideration of Quantum Backreaction effect. Therefore, the improvement of CPA is worthy to be studied further.

In surface hopping method, the excited-state carrier is on a single electronic state at the beginning of evolution, then the coherent electronic states are generated along with the evolution.[16] Coherent superposed electronic state pairs can be formed during ultrafast carrier transfer and the intra-band charge relaxation. While the coherent states tend to collapse back to a single electronic state induced by the disturbance of the external environment, which called quantum decoherence. The decoherence effect should be considered if it is faster than quantum transitions. The phonon-induced decoherence time related to the photocarrier recombination process is calculated using optical response theory, in which the pure-dephasing functions are fitted by:[17]

$$D(t) = exp(i\omega t)\,\langle exp\left(-\frac{i}{\hbar}\int_0^t \Delta E(\tau)\,d\tau\right)\rangle \quad (8)$$

in which $\langle\cdots\rangle$ represents the ensemble average, and $\omega = \Delta E/\hbar$. The above expression can be approximated by the second-order cumulant expansion:

$$D(t) = exp\left(-\frac{1}{\hbar^2}\int_0^t d\tau_1 \int_0^t d\tau_1\,\langle \Delta E(\tau)\Delta E(0)\rangle\right) \quad (9)$$

where $\langle \Delta E(\tau)\Delta E(0)\rangle$

$$C(t) = \langle \Delta E(\tau)\Delta E(0)\rangle \quad (10)$$

is the autocorrelation function (ACF) of unnormalized energy gap fluctuations. A Gaussian fit to the $D(t)$ decoherence function can gives the decoherence time. The shorter decoherence time, the more significant the decoherence effect between electronic states more pronounced.[18] The Frontier transform of the unnormalized ACF

can be calculated to obtain the phonon-induced spectral density:

$$I(\omega) = \left| \frac{1}{\sqrt{2\pi}} \int_{-\infty}^{\infty} dt e^{-i\omega t} C(t) \right|^2 \tag{11}$$

which indicates the frequency of the phonon modes coupled to the involving pair of states, and the amplitude at each frequency characterizes the strength of the vibration modes involved in electron-phonon coupling during photoinduced carrier separation and recombination dynamics.

2. Constructed supercells and the K-point sampling adopted by band unfolding method

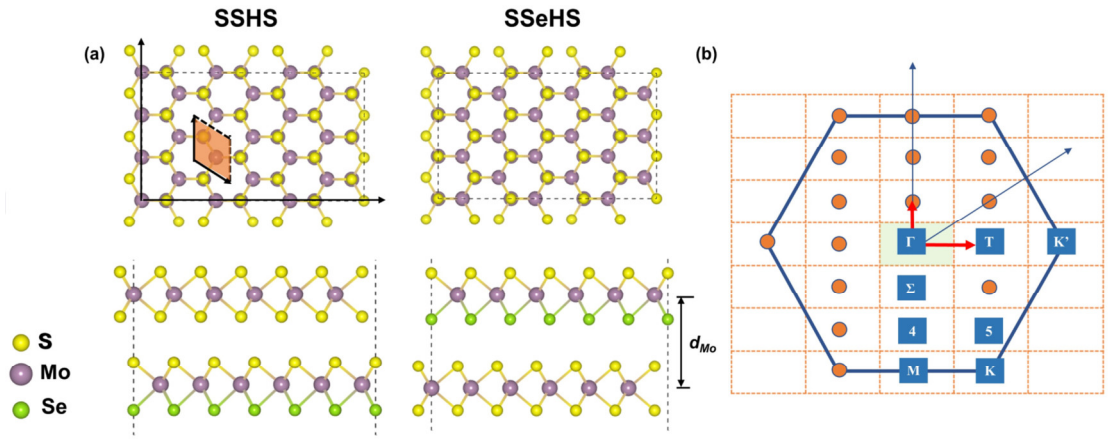

Fig. S1 (a) Top and side views of the Janus MoSSe/ MoS_2 heterobilayers with S-S and S-Se oriented interfaces, donated as SSHS and SSeHS. The orange shaded area is the primitive cell. (b) The Brillouin zone K points sampling of orthogonal supercell, the irreducible K points are marked in the diagram.

The orange shaded area in Fig. S1(a) is the (1×1) primitive cell, which is used to calculate the band structures, photocatalytic properties and optical absorption. For NAMD simulations, the (3×3) supercells in rectangle shape containing 108 atoms of Janus-MoSSe/ MoS_2 heterostructures with S/S and S/Se interfacial composition were constructed to model bilayers with only a single k-point (Γ point) for integration in the Brillouin zone, as shown in the area framed by the black dash lines in Fig. S1(a). The

K-points of primitive Brillouin zone are presented in Fig. S1(b), in which seven effective irreducible K points (Γ, Σ, 4, M, K, 5, T) are involved in the interlayer carrier transfer dynamics. The momentum of different electronic states relative to the photoexcited states especially the K and T points is determined by unfolding the energy bands.[19]

3. The relative energy calculation of the heterostructures for different stacking

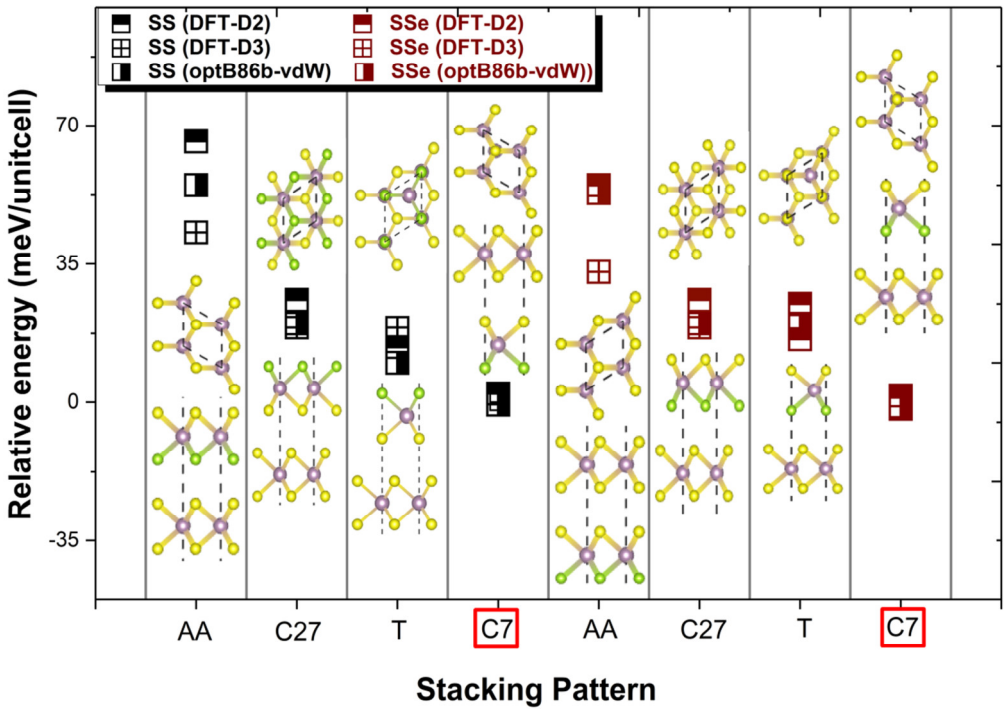

Fig. S2 The relative energy of the SSHS and SSeHS with four different typical stacking (i. e., AA, C27, T, C7). Insets are the top view and side view of the separate stacking geometries. The DFT-D2, DFT-D3 and optB86b-vdw methods are employed to describe the effect of the van der Waals (vdW) interaction.

4. The geometrical parameters of MoS_2 bilayers (MoS_2HS), SSHS and SSeHS

Table S1 Calculated geometrical parameters, the band gaps and the formation energy of the MoS_2 bilayers (MoS_2HS), SSHS and SSeHS primitive cells.

	Lattice parameter (Å)	**d_{Mo}(Å)**	**Bond length (Å)**			**Band gap(eV)**			**Formation energy (eV/unit)**
			Mo-S (MoS_2)	Mo-S (MoSSe)	Mo-Se (MoSSe)	PBE	HSE	PBE+SOC	
MoS_2HS	3.16	6.20	2.42	-	-	1.21	1.87	1.19	-0.33
SSHS	3.20	6.16	2.41	2.40	2.54	1.02	1.50	1.00	-0.24
SSeHS	3.20	6.51	2.41	2.40	2.54	0.93	1.35	0.85	-0.25

5. Coulombic Ion-dipole force and Bader charge analysis

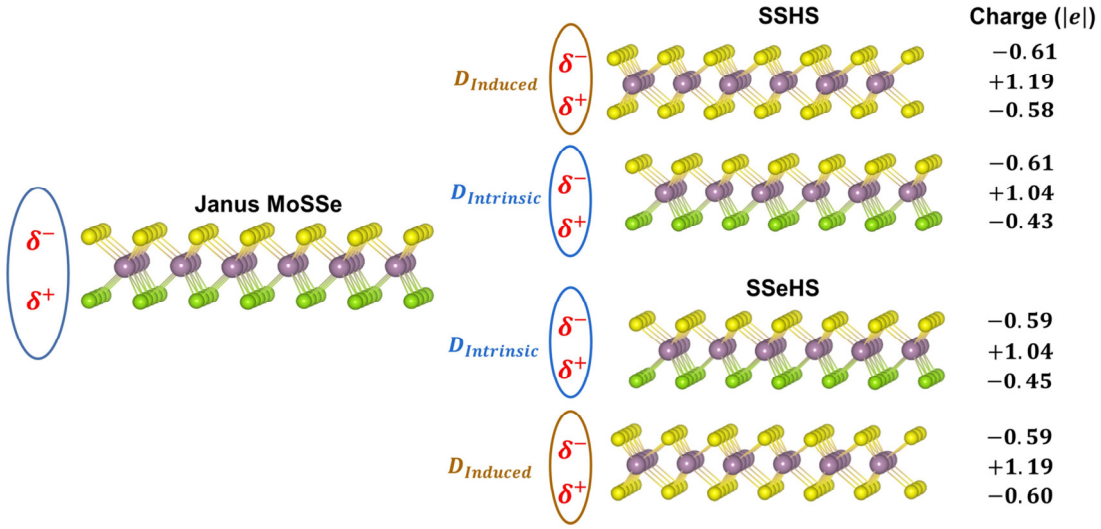

Fig. S3 Schematic illustration of the dipole moments for janus MoSSe monolayer, SSHS and SSeHS. The charge of ions in bottom, middle and top layers is obtained by Bader charge analysis, presented in the right side. Here, the positive (negative) value indicates that the ion in different layers possesses positive (negative) charges.

The charge redistribution in heterostructures is analyzed by the charge of ions, adopting the Bader program developed by Henkelman group.[20] Notable is, the Bader analysis assumes that charge density maxima are located at atomic centers (or at pseudoatoms), which matches the complete wave function throughout the atomic

augmentation sphere region. Therefore, it is necessary to perform the Bader analysis of electron density conducted on the reconstructed (all-electron) valence density. The reconstructed charge density in real space was generated from the converged DFT calculation.[21] However, the obtained results revealed that the difference between the charge of ions in heterostructures obtained by the two methods is marginal, that the methodology of Bader analysis has little effect on our main conclusions on the interfacial coupling effects.

6. Charge density difference of the heterostructures

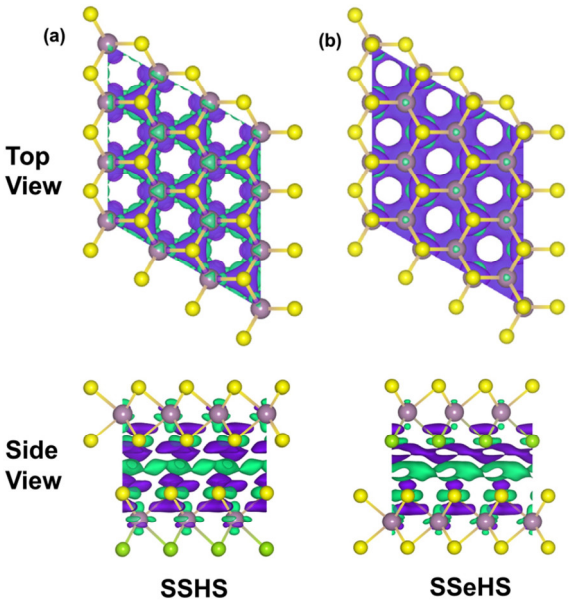

Fig. S4 Top and side views of charge density differences for SSHS (a) and SSeHS (b) heterostructures. The purple and green isosurfaces correspond to the charge depletion and accumulation.

The built-in interfacial E-field is formed by means of the charge rearrangement including charge depletion and accumulation across the heterojuction. As shown in Fig. S4, for SSeHS, electrons distributed in MoS_2 layer are more prefer to accumulate near the Mo atoms than the electrons distributed in MoSSe. In contrast, for SSHS, Mo atoms in MoS_2 layer have less electron accumulation than Mo atoms in MoSSe. Compared with SSHS, there is more electron accumulation at the sulfur atom near the MoS_2 layer

and more electron depletion at the selenium atom near the MoSSe layer in SSeHS. The charge density differences can also demonstrate the direction of the interfacial E-field, i.e., the E-field in SSHS points from MoS_2 to MoSSe while E-field in SSeHS points from MoSSe to MoS_2.

7. Photogenerated charge separation dynamics

7.1 Time-dependent energies of the Kohn-sham electronic states in momentum space

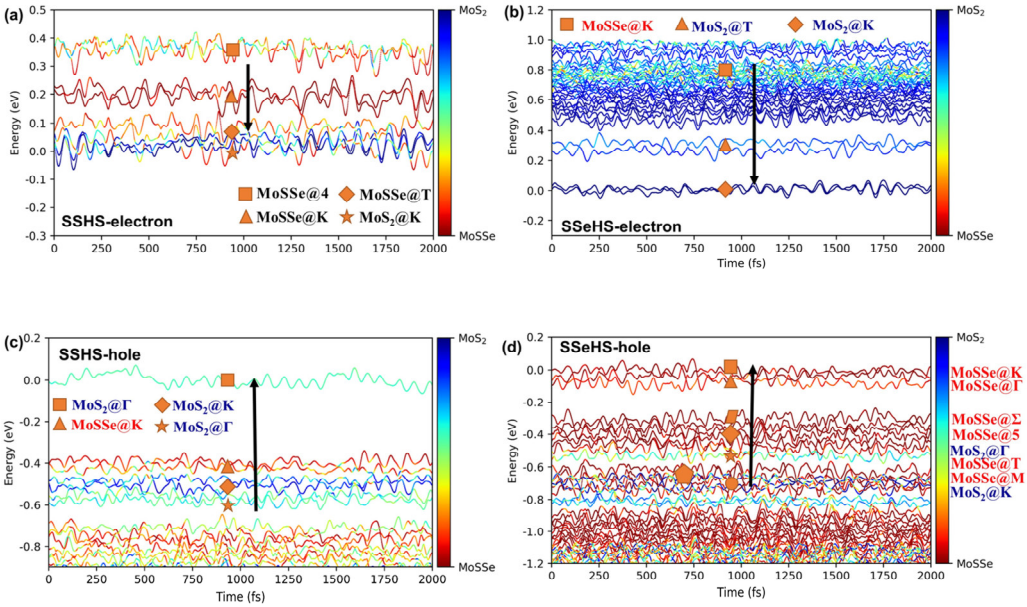

Fig. S5 Time evolutions of the energy states near the CBM for the SSHS and SSeHS (a)-(b), and the energy states near VBM for SSHS and SSeHS (c)-(d) respectively, and the color map indicates the orbital localization. The black arrows indicate the direction of carrier transfer.

Before exploring the photogenerated ultrafast carrier transfer dynamics, we analyzed in detail the energy evolutions of the states near CBM and VBM in SSHS and SSeHS. As depicted in Fig. S5, the MoS_2 and MoSSe components are expressed by the deep bule and red lines and thus the color of lines can reflect the hybridization of the energy orbitals. The amplitude of eigenenergy oscillation of SSHS is close to that of SSeHS, which can be attributed to that SSHS and SSeHS have similar phonon modes

by excited thermally.

For SSHS, the CBM energy states (MoS_2@K) are presented by two deep bule lines shown in Fig. S5(a), oscillating around 0eV. In the range of [0, 0.1] eV, the two light red lines overlapping with CBM represent the VB energy states at T point on MoSSe (MoSSe@T). In the vicinity of 0.2eV, there are two red lines, implicating that the orbitals are mainly distributed in MoSSe layer and the wave vector in the reciprocal space is K (MoSSe@K). Near 0.38eV, there exist two light red line, corresponding to the MoSSe@4 state, because there are only two 4 points in the whole Brillouin zone that can be folded to Γ point, and the two 4 points are not satisfying $e^{i(\overrightarrow{k_1}-\overrightarrow{k_2})\vec{R}} = 1$. For the electron transfer at the interface in SSHS, the photoexcited electron was initially located at the MoSSe@K or MoSSe@4 states, corresponding to the direct and indirect excitation cases respectively. While for SSeHS (Fig. S5 (b)), there are two deep blue lines near 0 eV, which represent the MoS_2@K state. The two energy levels with light blue coloring crossing around 0.3eV represents the MoS_2@T state. Oscillating around 0.8eV, there are two hybridized orbital states at the deep energy level, which correspond to the CBM states of MoSSe constituent layer (MoSSe@K). MoSSe@K is set as the initial state of the electron transfer for SSeHS.

Fig. S5 (c) indicates the time evolutions of energy states near VBM for SSHS, there are two light green lines around 0.6eV, representing the energy state at Γ point on MoS_2 layer below the VBM state. In the range of [-0.5, -0.4] eV, the two blue lines and two red lines from bottom to top stand for the MoS_2@K and MoSSe@K respectively. In addition, the energy at the VBM state has an oscillation of about 0.1eV, shown by the single light green line (MoS_2@Γ). In NAMD simulation, we assume that the photoexcited hole was initially populated at the MoSSe@K or MoS_2@K in order to understand the different relaxation channels of hole. For SSeHS, the oscillation of the Kohn-Sham eigenenergy is clearly revealed in Fig. S5 (d). The corresponding energy states are all listed in the right side and will not described in detail. Thereinto, there are strong orbital hybridization and energy level crossing around 0.55eV and 0.7eV, in which corresponds to MoS_2@Γ and MoS_2@K states. The two states are selected as the

distinct initial states for hole transfer in SSeHS to proceed the following direct and indirect carrier excitation in NAMD simulation.

7.2 Time evolution of the selected electronic states occupation in hole transfer of SSeHS

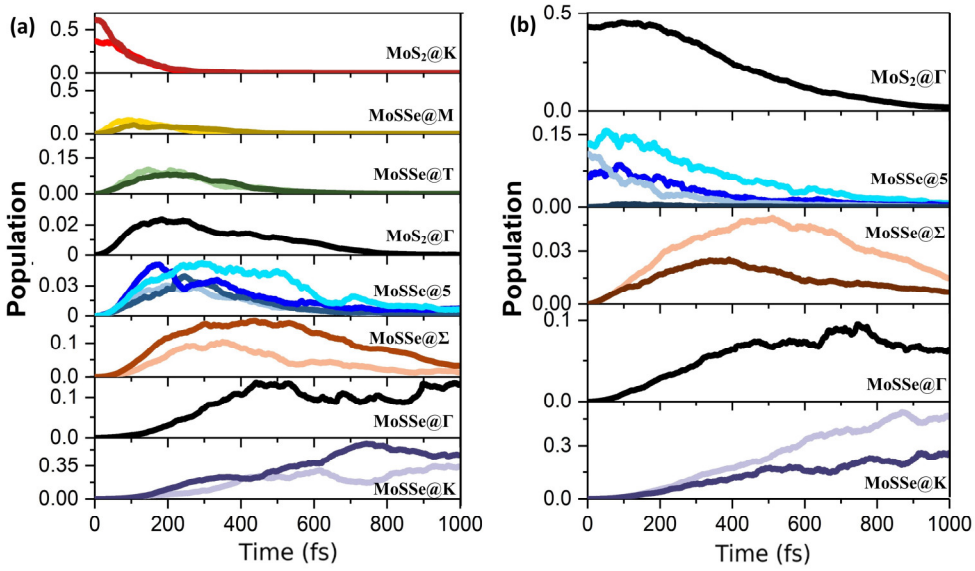

Fig. S6 The time-dependent occupation of the selected electronic states during the photogenerated hole transfer in SSeHS, the photoexcited hole is initially populated at MoS_2@K (a) and MoS_2@Γ (b)

8. Nonadiabatic e-h recombination dynamics by scissor correction

In the case of electron-hole recombination, NAC is inversely proportional to the energy difference, i.e., the band gap value. The $\langle \varphi_i | \nabla_R H | \varphi_j \rangle$ is determined by the electron-hole coupling and the wavefunction overlapping between CBM and VBM states. Here, we scaled the PBE energy gaps to the corresponding HSE06 values by scissor correction[22] and repeated the NAMD calculations of carrier recombination, the results are presented in Fig. S7. It is found that the e-h recombination times obtained by HSE06 are 1107 ps and 4697 ps for SSHS and SSeHS respectively, which is about 1.4 times longer than that of the PBE results. In general, PBE functional excessively facilitates the wavefunction delocalization between donor-acceptor electronic states

compared with hybrid functionals in larger condensed matter systems, decreasing the NAC strength due to the delocalization-weaken electron-phonon coupling effect.[23] Therefore, the difference in NAC appears to be relatively small between the PBE and HSE06 results in our work. As expected, the introduction of HSE06 functional only changes the timescale of photogenerated carrier recombination but have no effect upon our conclusion.

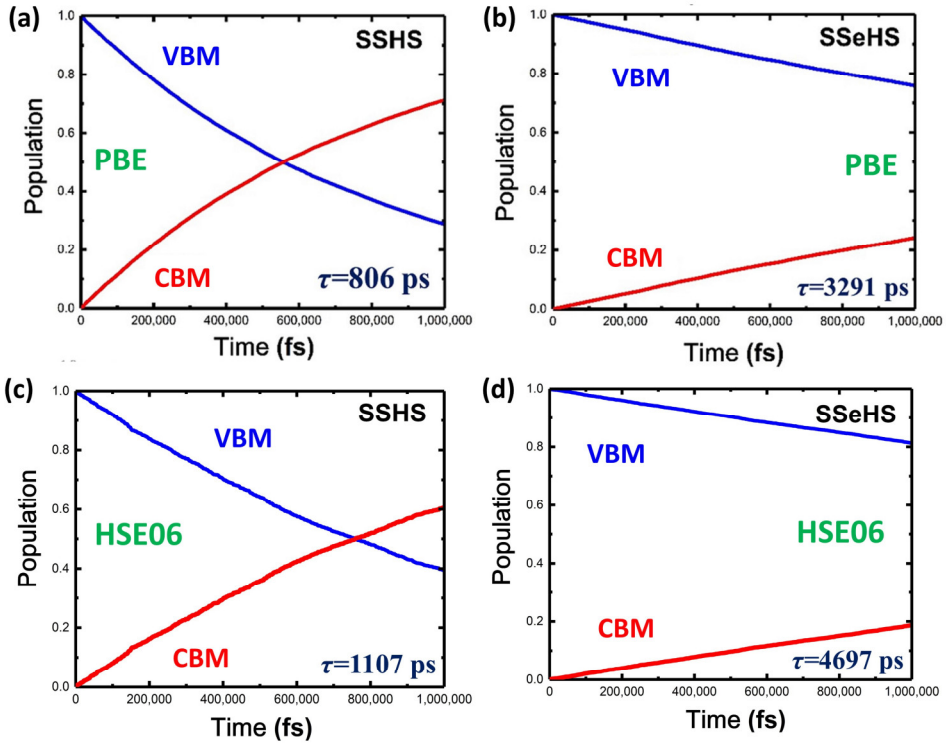

Fig. S7 Nonadiabatic e-h recombination dynamics in SSHS and SSeHS. The initial state corresponds to the electron excitation from the VBM to CBM states. Time evolution of the excited and ground states population are indicated by blue and red lines respectively. The PBE (a)-(b) and the HSE06 (c)-(d) results are included.

9. Calculation details about solar-to-hydrogen (STH) efficiency

According to the previous calculation methodology,[24, 25] the STH efficiency (η_{STH}) is determined by the product of the energy conversion efficiency of light absorption (η_{abs}) and the carrier utilization (η_{cu}):

$$\eta_{\mathrm{STH}} = \eta_{\mathrm{abs}} \times \eta_{\mathrm{cu}} \tag{12}$$

Here, η_{abs} are calculated by the following expression:

$$\eta_{\text{abs}} = \frac{\int_{E_g}^{\infty} P(\hbar\omega) d(\hbar\omega)}{\int_{0}^{\infty} P(\hbar\omega) d(\hbar\omega)} \tag{13}$$

where $P(\hbar\omega)$ and E_g are the AM1.5G solar energy flux as a functional of the photo energy $\hbar\omega$ and the band gap of the photocatalyst. While the efficiency of carrier utilization (η_{cu}) is defined as:

$$\eta_{\text{cu}} = \frac{\Delta G_{H_2O} \int_{E}^{\infty} \frac{P(\hbar\omega)}{\hbar\omega} d(\hbar\omega)}{\int_{E_g}^{\infty} P(\hbar\omega) d(\hbar\omega)} \tag{14}$$

where ΔG_{H_2O} is the free energy of 1.23eV for water splitting and the term of $\int_{E}^{\infty} \frac{P(\hbar\omega)}{\hbar\omega} d(\hbar\omega)$ represents the effective photocurrent density. Inside, E represents the energy of photons that can actually be used in the water splitting process, defined as:

$$E = \begin{cases} E_g, (\chi(\mathrm{H_2}) \geq 0.2, \chi(\mathrm{O_2}) \geq 0.6) \\ E_g + 0.2 - \chi(\mathrm{H_2}), (\chi(\mathrm{H_2}) < 0.2, \chi(\mathrm{O_2}) \geq 0.6) \\ E_g + 0.6 - \chi(\mathrm{O_2}), (\chi(\mathrm{H_2}) \geq 0.2, \chi(\mathrm{O_2}) < 0.6) \\ E_g + 0.8 - \chi(\mathrm{H_2}) - \chi(\mathrm{O_2}), (\chi(\mathrm{H_2}) < 0.2, \chi(\mathrm{O_2}) < 0.6) \end{cases} \tag{15}$$

where $\chi(\mathrm{H_2})$and $\chi(\mathrm{O_2})$are overpotentials for HER and OER calculated by HSE hybrid functional respectively.

10. The investigation of light absorption performance.

We perform the investigation of the optical absorptions for SSHS and SSeHS by employing HSE06 functional. The calculation of optical properties is divided into two steps. Firstly, the frequency-dependent dielectric function $\varepsilon(\omega)$ is obtained by following expression:

$$\varepsilon(\omega) = \varepsilon_r(\omega) + i\varepsilon_i(\omega) \tag{16}$$

where the $\varepsilon_r(\omega)$ and $\varepsilon_i(\omega)$ are the real and imaginary parts respectively. The $\varepsilon_i(\omega)$ is calculated as follows:

$$\varepsilon_i(\omega) = \frac{2e^2\pi}{\Omega\varepsilon_0} \sum_{c,v,\vec{k}} \left|\langle c, \vec{k} \left| \vec{u} \cdot \vec{k} \right| v, \vec{k} \rangle\right|^2 \delta\left(E_{c,\vec{k}} - E_{v,\vec{k}} - \hbar\omega\right) \tag{17}$$

in which the c and v indicate the conduction and valence band states, and u represent the supercell periodic part of the orbitals at K-points. Then the optical absorption coefficients of heterostructures are evaluated by the following formula:[26]

$$\alpha(\omega) = \frac{\sqrt{2}\omega}{c}\left\{[\varepsilon_r(\omega)^2 + \varepsilon_i(\omega)^2]^{1/2} - \varepsilon_r(\omega)\right\}^{1/2} \quad (18)$$

Since the light absorption in the low-energy region where the polarization direction is perpendicular to the 2D nanosheet plane is always weak, we mainly focus on the light absorption where the polarization direction is parallel to the heterostructures plane. Due to the structural anisotropy, the corresponding $\alpha(\omega)$ is mainly contributed by the $\alpha(\omega)^{xx}$ and $\alpha(\omega)^{yy}$ components and satisfies $\alpha(\omega)^{xx} = \alpha(\omega)^{yy}$.

Reference

1. R. Crespo-Otero and M. Barbatti, *Chemical Reviews*, 2018, **118**, 7026-7068.
2. Q. Zheng, W. Chu, C. Zhao, L. Zhang, H. Guo, Y. Wang, X. Jiang and J. Zhao, *WIREs Computational Molecular Science*, 2019, **9**, e1411.
3. M. Richter, P. Marquetand, J. González-Vázquez, I. Sola and L. González, *Journal of Chemical Theory and Computation*, 2012, **8**, 374-374.
4. H. M. Jaeger, S. Fischer and O. V. Prezhdo, *The Journal of Chemical Physics*, 2012, **137**, 22A545.
5. E. Runge and E. K. U. Gross, *Physical Review Letters*, 1984, **52**, 997-1000.
6. C. M. Isborn, X. Li and J. C. Tully, *The Journal of Chemical Physics*, 2007, **126**, 134307.
7. W. Kohn and L. J. Sham, *Physical Review*, 1965, **140**, A1133-A1138.
8. I. Tavernelli, B. F. E. Curchod and U. Rothlisberger, *The Journal of Chemical Physics*, 2009, **131**, 196101.
9. C. Hu, H. Hirai and O. Sugino, *The Journal of Chemical Physics*, 2008, **128**, 154111.
10. P. V. Parandekar and J. C. Tully, *The Journal of Chemical Physics*, 2005, **122**, 094102.
11. C. F. Craig, W. R. Duncan and O. V. Prezhdo, *Physical Review Letters*, 2005, **95**, 163001.
12. L. Wang, A. Akimov and O. V. Prezhdo, *The Journal of Physical Chemistry Letters*, 2016, **7**, 2100-2112.
13. A. V. Akimov and O. V. Prezhdo, *Journal of Chemical Theory and Computation*, 2013, **9**, 4959-4972.
14. X.-Y. Liu, X.-Y. Xie, W.-H. Fang and G. Cui, *The Journal of Physical Chemistry A*, 2018, **122**, 9587-9596.
15. R. Long, O. V. Prezhdo and W. Fang, *WIREs Computational Molecular Science*, 2017, **7**, e1305.
16. R. Long and O. V. Prezhdo, *Nano Letters*, 2015, **15**, 4274-4281.
17. S. Mukamel, 1995.
18. A. V. Akimov and O. V. Prezhdo, *The Journal of Physical Chemistry Letters*, 2013, **4**, 3857-3864.

19. V. Popescu and A. Zunger, *Physical Review B*, 2012, **85**, 085201.
20. W. Tang, E. Sanville and G. Henkelman, *Journal of Physics: Condensed Matter*, 2009, **21**, 084204.
21. E. Aubert, S. Lebègue, M. Marsman, T. T. T. Bui, C. Jelsch, S. Dahaoui, E. Espinosa and J. G. Ángyán, *The Journal of Physical Chemistry A*, 2011, **115**, 14484-14494.
22. C. Y. Wang, P. Elliott, S. Sharma and J. K. Dewhurst, *Journal of Physics: Condensed Matter*, 2019, **31**, 214002.
23. L. Zhang, W. Chu, Q. Zheng, A. V. Benderskii, O. V. Prezhdo and J. Zhao, *The Journal of Physical Chemistry Letters*, 2019, **10**, 6151-6158.
24. Z. Chen, T. F. Jaramillo, T. G. Deutsch, A. Kleiman-Shwarsctein, A. J. Forman, N. Gaillard, R. Garland, K. Takanabe, C. Heske, M. Sunkara, E. W. McFarland, K. Domen, E. L. Miller, J. A. Turner and H. N. Dinh, *Journal of Materials Research*, 2011, **25**, 3-16.
25. M. Sun and U. Schwingenschlögl, *Chemistry of Materials*, 2020, **32**, 4795-4800.
26. M. Sun, J.-P. Chou, J. Gao, Y. Cheng, A. Hu, W. Tang and G. Zhang, *ACS Omega*, 2018, **3**, 8514-8520.